Electronic Supplementary Material (ESI) for Materials Horizons. This journal is © The Royal Society of Chemistry 2019

Supporting Information for

Giant shape memory and domain memory effects in antiferroelectric single crystals

Fangping Zhuo[a,b], Dragan Damjanovic[b], Qiang Li[a,*], Yaming Zhou[a], Yongjie Ji[a], Qingfeng Yan[a], Yiling Zhang[c], Yun Zhou[a], and Xiangcheng Chu[c]

[a]*Department of Chemistry, Tsinghua University, Beijing 100084, China*

[b]*Group for Ferroelectrics and Functional Materials, Institute of Materials, Swiss Federal Institute of Technology in Lausanne—EPFL, CH-1015 Lausanne, Switzerland*

[c]*State Key Laboratory of New Ceramics and Fine Processing, Tsinghua University, Beijing 100084, China*

**Corresponding author: qiangli@mail.tsinghua.edu.cn*

This PDF file includes:

Figures S1 to S11

Movies S1 and S2

Table S1

References 1 to 12

1: Crystal growth

In this work, $Pb_{0.97}La_{0.02}(Zr_{0.66}Sn_{0.23}Ti_{0.07})O_3$ were chosen as the starting composition. Raw oxides of PbO, La_2O_3, TiO_2, ZrO_2 and SnO_2 with high purity (99.99%) were weighted out according to the stoichiometric ratio. $Pb_{0.97}La_{0.02}(Zr_{0.66}Sn_{0.23}Ti_{0.07})O_3$ powder was ball-milled for 6 h. Then, the as-prepared mixtures were calcined at about 1100 °C to obtain the perovskite phase *via* the conventional solid-state method.

A self-designed heating tubular furnace was used for flux growth. A Platinum crucible, filled with $PbO–PbF_2–B_2O_3$ flux and the calcined PLZST powders, was placed on a firebrick. Then, the mixed powders were heated up to 1200 °C to make the homogeneous solution melt. The solution was cooled down at a rate of 1~10 °C/h to ~800 °C and finally furnace-cooled to room temperature. It usually takes 300~500 hours to grow the PLZST single crystals. The as-grown PLZST single crystals were separated from the solidified flux.

2: Crystal structure and field-induced phase transformations

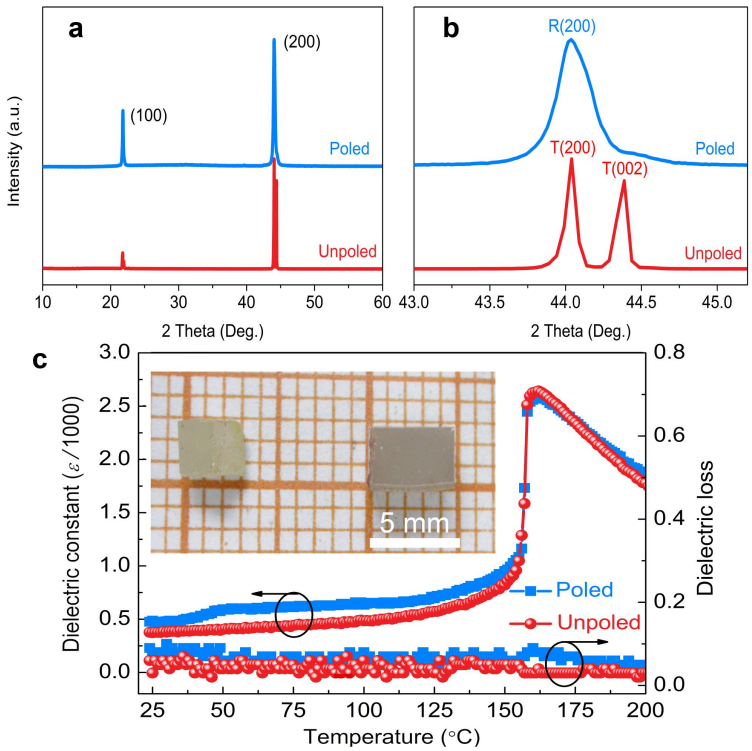

Fig. S1. (a) Room temperature XRD patterns of the unpoled and poled [001]-oriented PLZST single crystals. (b) Details of the region around (200) peaks. (c) Temperature-dependent dielectric constant and loss of the unpoled and poled samples at 10 kHz. The inset shows the images of the as-grown PLZST single crystals.

The poled single crystal was polarized at room temperature under an electric field of 50 kV cm^{-1} for 5 min in silicon oil. The as-prepared samples were well oriented along the [001] direction, as shown in Fig. S1a. Two separated T(002) and T(200) peaks were found by X-ray diffraction in the unpoled crystal (Fig. S1b), indicating a tetragonal AFE (AFE_T) structure[1]. However, only a single R(200) peak emerged in the poled crystal (Fig. S1b), which reveals a rhombohedral FE (FE_R) phase.[1] Fig. S1c plots the temperature-dependent dielectric properties for unpoled and poled PLZST crystals. The unpoled sample exhibits AFE_T phase at room temperature, which transforms to nonpolar cubic paraelectric phase at Curie point T_C (163 °C). For the poled sample, the field induced FE_R phase transforms back to AFE_T phase at ~50 °C, the temperature where an anomaly is observed in the dielectric permittivity (Figure S1c), which is known as the depolarization temperature (T_d),[2] and then to paraelectric phase at 163 °C.

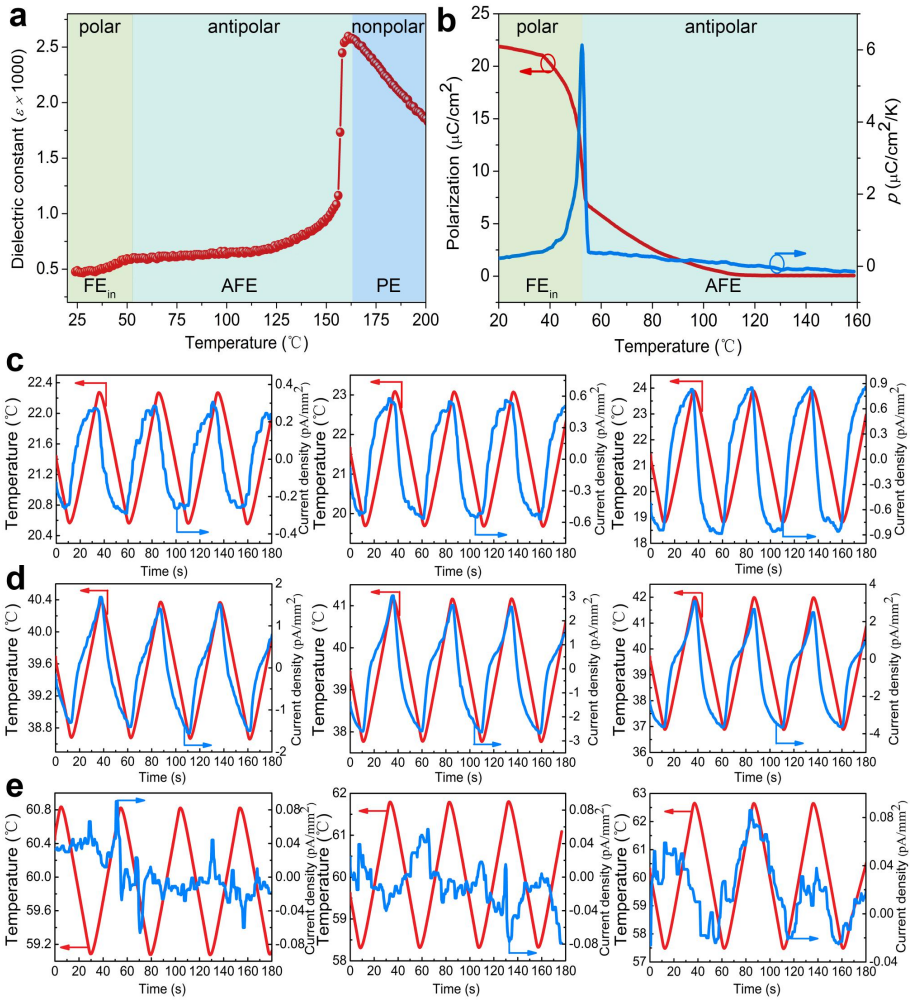

Fig. S2. (a) Temperature-dependent dielectric permittivity of the poled crystal at 10 kHz. (b) Temperature-dependent pyroelectric coefficient (p) and corresponding polarization of the poled PLZST single crystal. A large pyroelectric coefficient (about 6 μC/cm^2/K) can be detected at the FE$_{in}$-to-AFE phase transition temperature, i.e., the T_d, which is accompanied by a large polarization change. Phase-sensitive measurements of the pyroelectric current were carried out by using a Keithley 486 picoammeter. The measured pyroelectric current densities near (c) 20 °C, (d) 40 °C, and (e) 60 °C at temperature oscillations. The emergency of pyroelectric current in poled sample at temperature below T_d reveals the evidence of induced FE phase. The amplitude of the measured pyroelectric current oscillation increases with the temperature oscillation increasing. When the temperature reaches 60 °C, no obvious modulation of the pyroelectric current, in response to a triangular temperature wave, can be detected in the AFE phase. Note that noise in the current might be related to the instability of background temperature wave and the background current fluctuations.

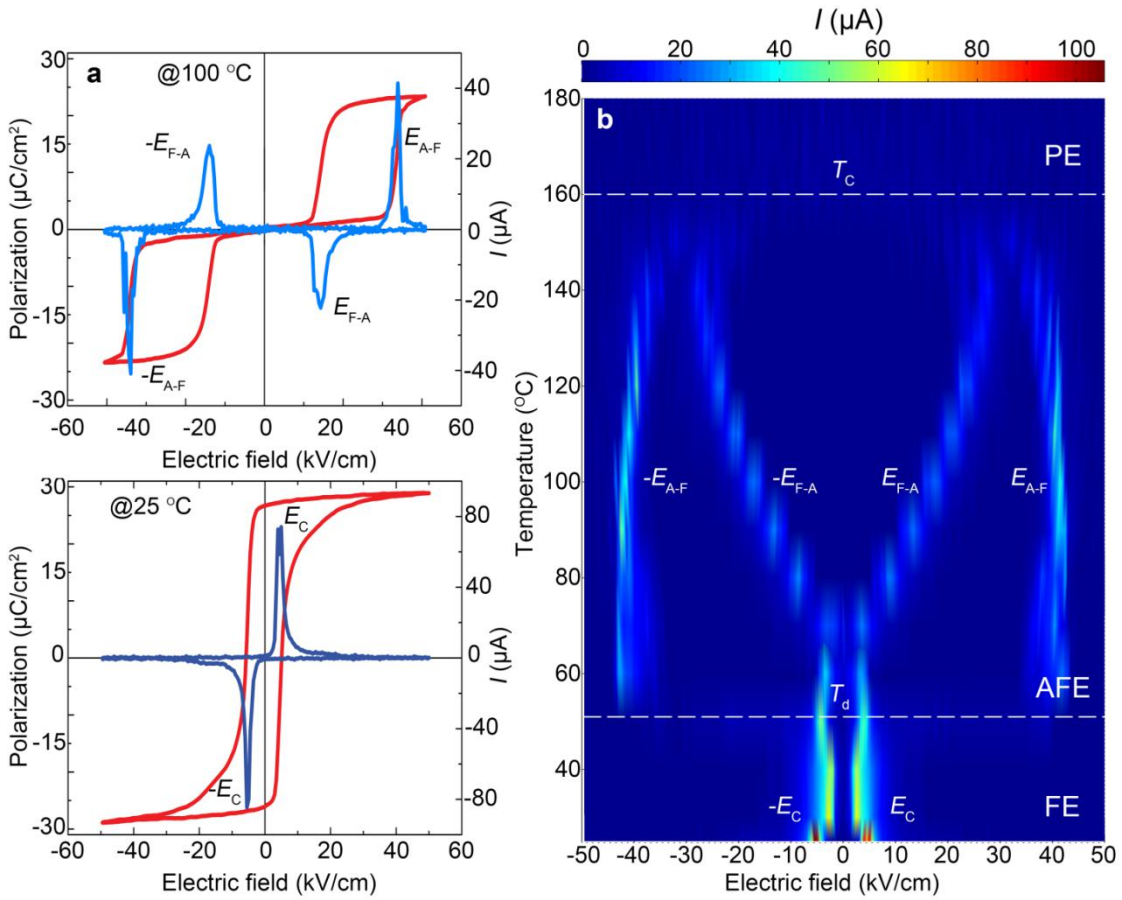

Fig. S3. (a) *P*–*E* hysteresis loops and corresponding current *vs* electric field (*I*–*E*) curves at 25 °C and 100 °C. (b) The contour map of *I*–*E* curves as a function of temperature for the PLZST crystal. The $-E_C$ and E_C mean the coercive electric fields, $-E_{A\text{-}F}$ and $E_{A\text{-}F}$ represent the critical switching electric fields of AFE to FE phase transition, $-E_{F\text{-}A}$ and $E_{F\text{-}A}$ refer to the critical switching electric fields of FE to AFE phase transition, respectively. The absolute value of *I* was taken to draw the contour map in (b).

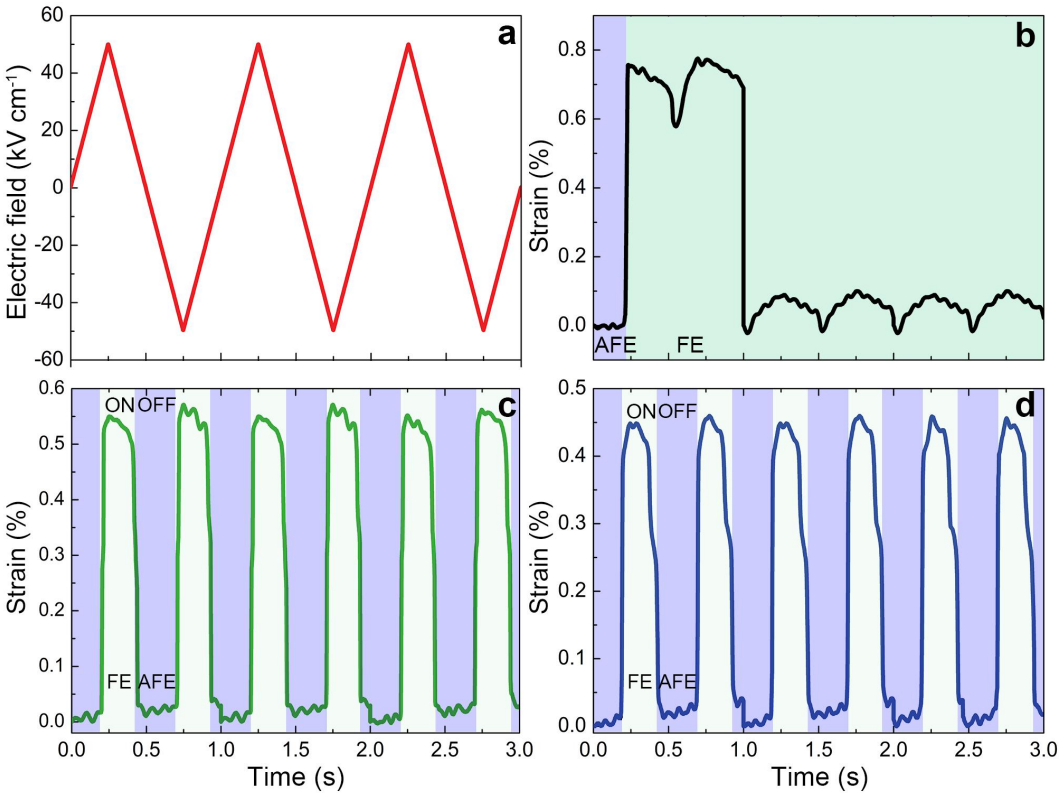

Fig. S4. Response timescale of electrostrain. (a) Triangular waveform with a maximum amplitude of 50 kV cm^{-1} for the strain measurements. Electrostrictive responses under the applied triangular bias field is shown for (b) 30 °C, (**c**) 100 °C and (d) 130 °C. The "ON"/"OFF" states in (c, d) are applied to show switching characteristic. All electrostrains were captured using TF 2000E ferroelectric tester equipped with a laser interferometer.

In order to evaluate the strain response for the PLZST single crystals, we applied a triangular waveform with a period of 1 s (Fig. S4a) and captured the corresponding strain with the TF2000E. At 30 °C, the electric-field-induced strain appears immediately once the field reaches the critical field of about 45 kV cm^{-1} (Fig. S4b). However, the electrostrictive performance is irrecoverable, as indicated by the sharply decreased strain after further electric field cycling (Fig. S4b). This phenomenon can be well understood by the shape memory effect and domain switching in the induced FE phase. The electrostrain of the PLZST crystals is recoverable when temperature is above T_d (see Fig. S4c and S4d measured at 100 °C and 130 °C, respectively). Clearly, the field-forced strain change between FE and AFE states exhibits a sharp increase at the forward field and an abrupt decrease at the backward field. Therefore, PLZST antiferroelectric single crystals may be developed for new concept actuators in aiming of achieving "digital displacement transducers", in which "ON" and "OFF" bistable strain states exhibit for a certain magnitude of electric field.

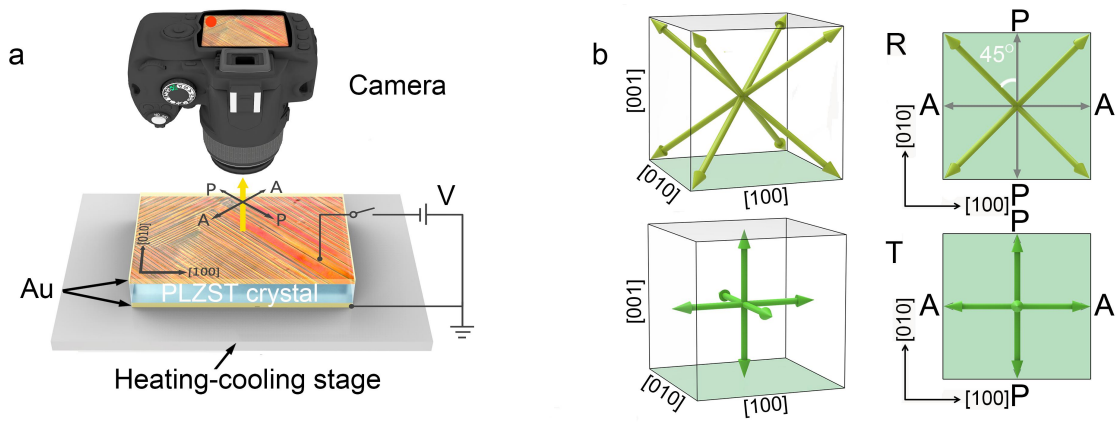

Fig. S5. (a) Schematic of the *in situ* PLM measurements. (b) Schematic of the P_S for R and T phases, and the variation of the P_S on the (001) surface.

For a rhombohedral (R) phase, there are eight possible spontaneous polarization (P_s) directions, along the <111> family of crystallographic directions (Fig. S5b). The projections of these P_s on the $(001)_C$ plane are along the <110> crystallographic directions, so that the R domains only have an extinction position at 45° when observing from [001] direction. There are six possible P_s for a tetragonal (T) phase, and the projections of these six P_s on the $(001)_C$ surface are shown in Fig.S5b. Therefore, the T domains have an extinction angle at 0° when observing the $(001)_C$ plane. Based on the extinction angles of the AFE tetragonal, and FE rhombohedral symmetry (see Table S1), we can distinguish the AFE tetragonal and FE rhombohedral phases for the [001]-oriented sample using the PLM measurements.

Table S1. Extinction angle for various symmetry with respect to crystal planes.

symmetry	extinction angle of (001) plane[a]	extinction angle of (011) plane[b]	extinction angle of (111) plane[c]
tetragonal	0°	0°	0°,30°,60°
rhombohedral	45°	0°,35.3°,54.7°	0°,30°,60°

[a]Reference directions [100] and [010]; [b]Reference directions $[1\,\bar{1}\,0]$ and [001]; [c]Reference directions $[\bar{1}\,\bar{1}\,2]$ and $[1\,\bar{1}\,0]$.

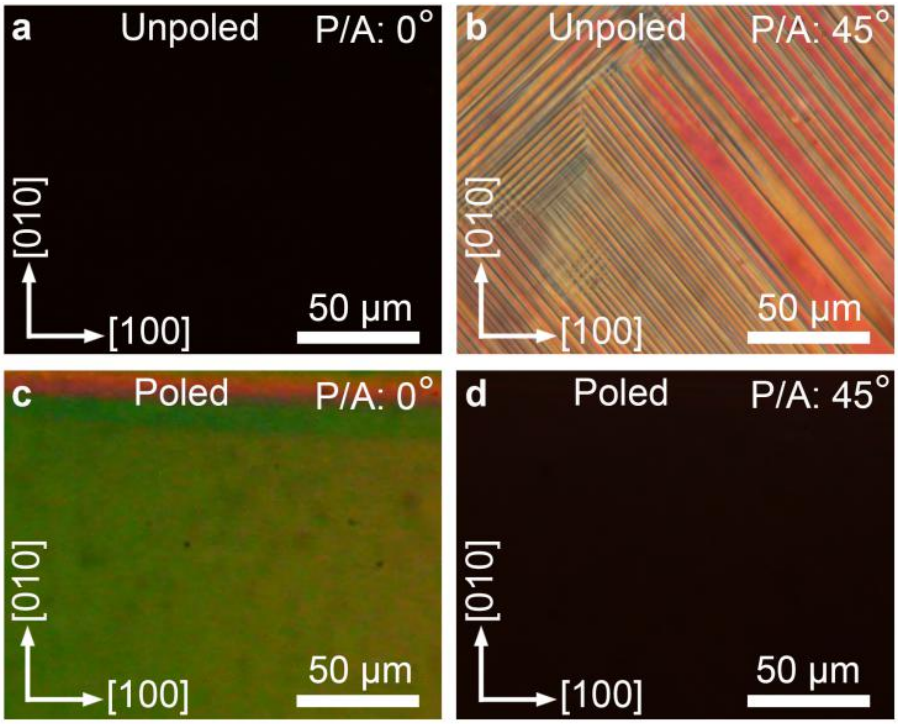

Fig. S6. Photographs of domain structures observed on the PLZST crystal at 30 °C. For the unpoled sample with the AFE T phase: (a) P/A=0° and (b) P/A=45°. For the poled sample with the FE R phase: (c) P/A=0° and (d) P/A=45°.

3: X-ray photoelectron spectroscopy

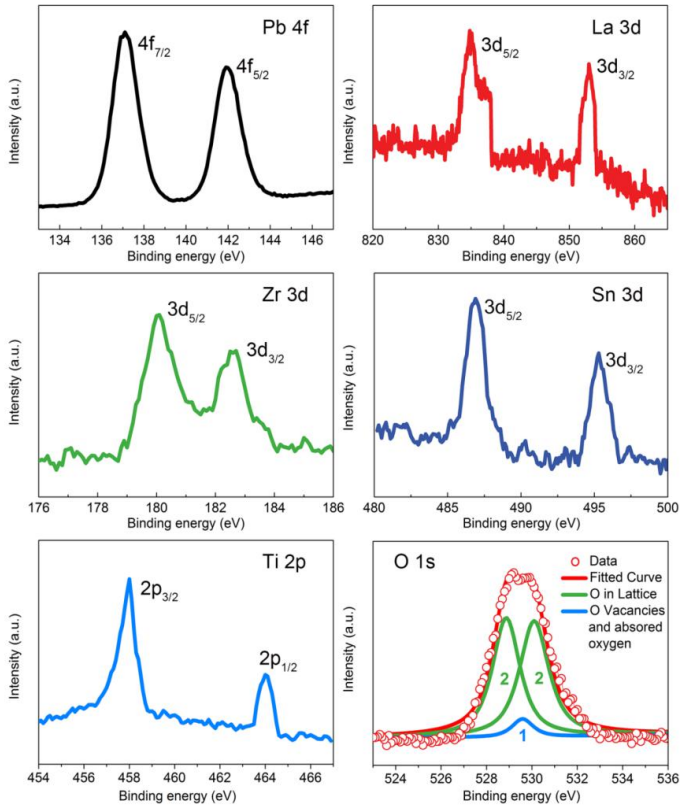

Fig. S7. High-resolution XPS spectra for the (Pb,La)(Zr,Sn,Ti)O_3 single crystal, Pb 4f, La 3d, Zr 3d, Sn 3d, Ti 2p and O 1s signals, respectively.

To support the phase-transition-mediated domain memory mechanism, further experiments based on the x-ray photoelectron spectroscopy (XPS) were carried out. Segments of XPS spectrum for the PLZST single crystal are plotted in Fig. S7. Obviously, they give the binding energies of 137.0 eV for Pb $4f_{7/2}$, 180.0 eV for Zr $3d_{5/2}$, and 487.0 eV for Sn $3d_{5/2}$, which are in agreement with the results in $PbZr_{0.96}Sn_{0.04}O_3$ antiferroelectric single crystal[3]. The binding energies of 836.0 eV for La $3d_{5/2}$ and 458.0 eV for Ti $2p_{3/2}$ are also obtained, which are in consistent with data reported elsewhere.[3,4] The O 1s signal and corresponding fitting curves can resolve two components. On one hand, the peaks of binding energies at 528.5 eV and 530.5 eV correspond to the oxygen in the PLZST lattice, including Pb-O, La-O, Zr-O, Sn-O, and Ti-O bonds. On the other hand, the binding energy of the component at about 529.6 eV refers to the oxygen vacancies in the crystal or chemically adsorbed oxygen on the crystal surfaces. Here, the ratio of areas under the corresponding peaks is usually used to determine the oxygen vacancy concentration and the ratio was calculated to be 0.08, suggesting a low oxygen vacancy concentration.

4: Irreversible and reversible domain switching at mesoscopic scale.

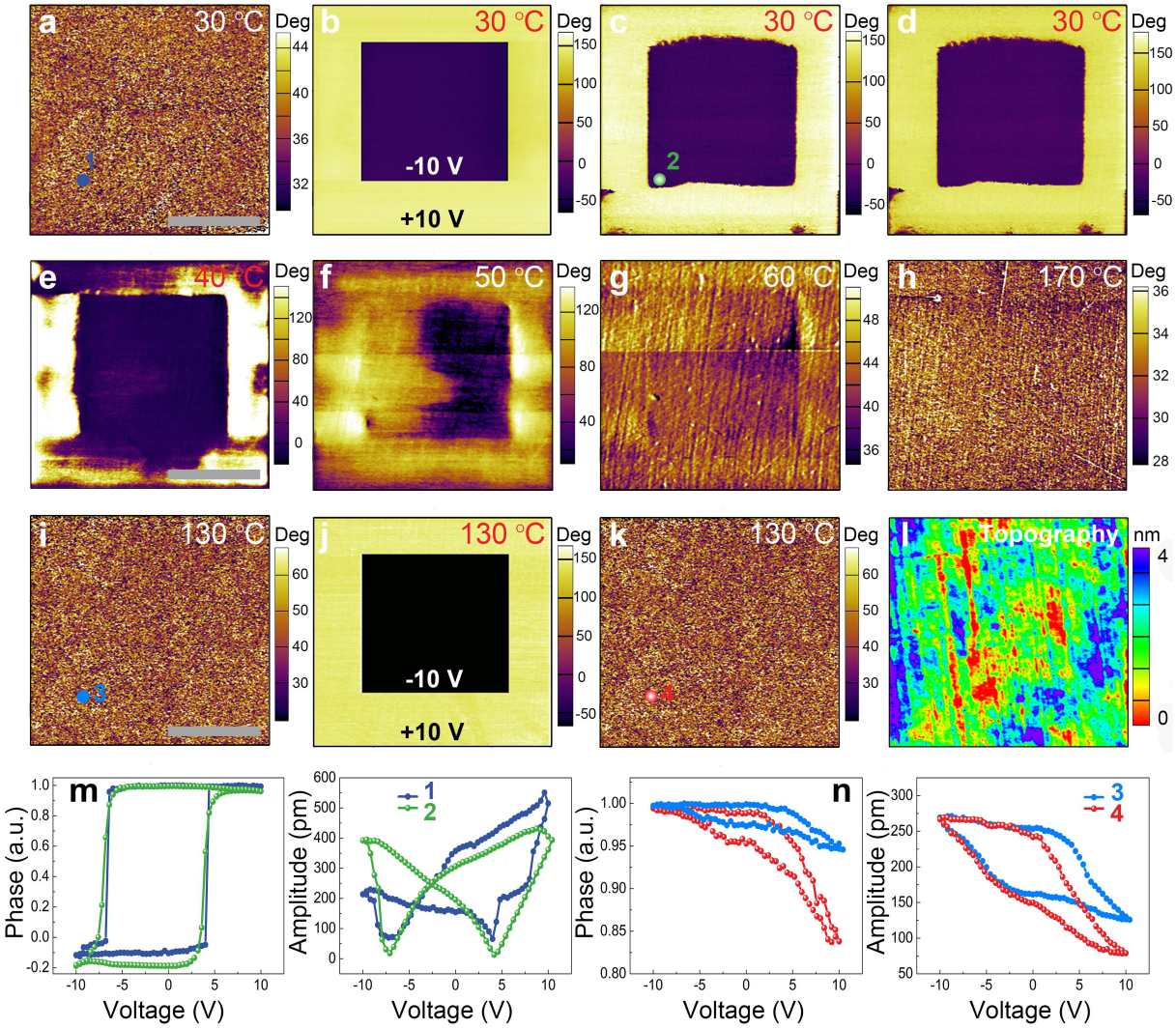

Fig. S8. The out-of-plane PFM phase images of the PLZST single crystal at 30 °C, which were taken (a) in the unpoled state, (b) taken after a probe bias of (+/–10 V), (c) taken immediately after the probe bias removal, and (d) taken after the removal of the bias for 2 hours. Temperature-dependent PFM phase images at (e) 40 °C, (f) 50 °C, (g) 60 °C, and (h) 170 °C. The PFM phase images of the crystal at 130 °C, which were taken (i) in the unpoled state, (j) taken after a probe bias of (+/–10 V), and (k) taken immediately after the bias removal. (l) The corresponding topography image at 130 °C. (m,n) Typical hysteresis loops measured on the locations as marked on (a,c) and (i,k). The scale bar is 2 μm.

In this work, the PFM was employed to explore the domain patterns and irreversible/reversible phase transitions for the PLZST AFE single crystals. No piezoelectric signal can been detected for the sample (see Fig. S8a), indicating its antiferroelectric nature.[5] In order to clarify the field-induced irreversible and reversible phase transitions, local poling

was carried out using PFM. When the probe biases of +/–10 V are applied to the sample, the appearance of a purple phase contrast (see Fig. S8b) represents the domain switching. Therefore, these results demonstrate that the polarization can be induced by applying a poling field on the antiferroelectric domains of this crystal. It is worth noting that the induced domains written in the selected area are capable of remaining switched after removal of the probe bias (see Fig. S8c,d), which confirms the electric field-induced irreversible phase transition. At temperatures lower than 50 °C, the induced ferroelectric domains are persistent (Fig. S8d,e). The depolarization is initiated at T_d of 50 °C (Fig. S8f) and is completely finalized at 60 °C (Fig. S8g). As the temperature reaches above T_C (163 °C), the antiferroelectric domains will transform into paraelectric domains (no response in the phase image Fig. S8h, consistent with the nonpolar character). To visualize the polarization switching of these antiferroelectric domains at 130 °C, the same probe biases of +/–10 V are subsequently applied. Clearly, a new purple phase contrast emerges and therefore reveals that the polarization in the domains of this crystal can also be induced (Fig. S8j). However, the field-induced domains switch back to antiferroelectric domains after the probe bias removal (compare Fig. S8i with Fig. S8k), which indicates that the field-induced AFE-FE phase transition is reversible. The topography (Fig. S8l) of the surface shows a stripe-like profile, reflecting the mesoscopic structure of PLZST. To test the polarization reversal behaviors, we recorded the local phase and amplitude loops by scanning the probe voltage from –10 to +10 V. A rectangular phase-voltage loop and corresponding butterfly amplitude-voltage loop are observed in the unpoled sample (see point 1 in Fig. S8a), suggesting the occurrence of ferroelectric polarization reversal.[5] Our results demonstrate that the local AFE phase can be transformed into FE phase. To confirm the induced FE phase, the hysteresis loops were then taken after the probe bias removal. Clearly, similar phase-voltage loop and corresponding amplitude-voltage loop are obtained (see point 2 in Fig. S8c), validating the induced FE phase. As a result, the AFE→FE phase transition is irreversible. At 130 °C, the hysteresis loops show a significant difference (compare Fig. S8n with Fig. S8m). No FE-like rectangular phase-voltage loop and butterfly-like amplitude-voltage loop can be detected, revealing the character of antiferroelectricity.

5: Structural model for incommensurate modulations in the PLZST single crystals

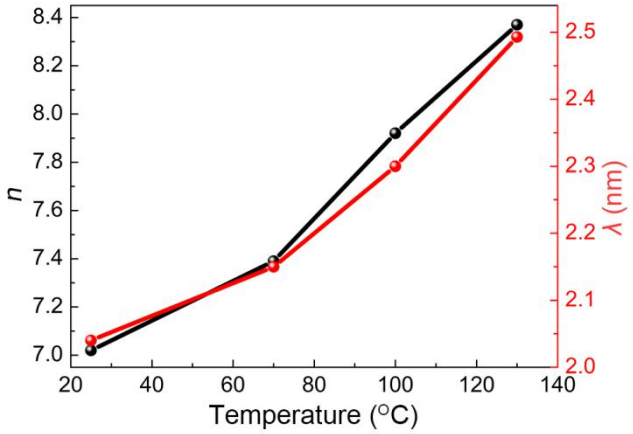

Fig. S9. The n in $H = h\mathrm{a}^* + k\mathrm{b}^* + l\mathrm{c}^* \pm (1/n)\boldsymbol{q}$ and modulation wavelength (λ) as a function of temperature.

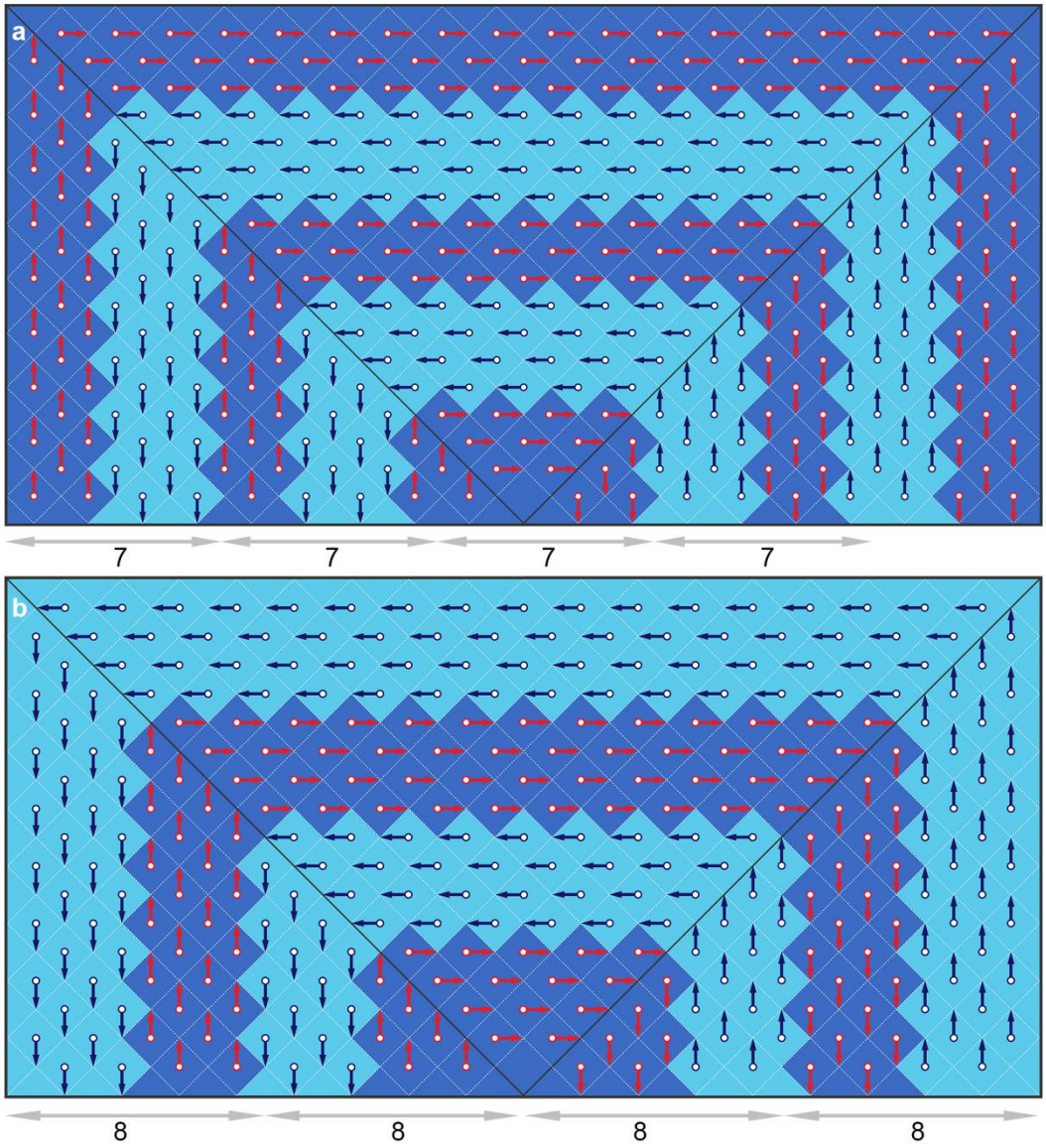

Fig. S10. Structure model of the intertwined 90° domain walls in PLZST single crystals with incommensurate modulations: (a)⋯7/7⋯ and (b) ⋯8/8⋯. All arrows show the Pb-cation displacements in the {110} plane of the tetragonal lattices.

6: Mechanism for the SME in antiferroelectric crystals

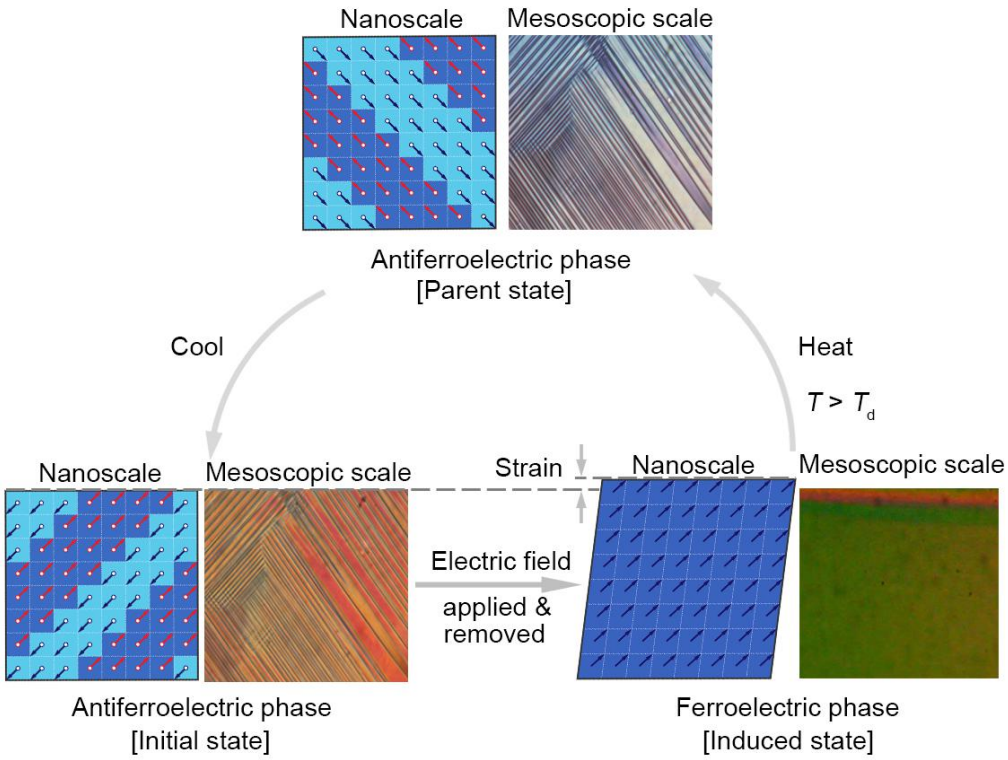

Fig. S11. The mechanism for the shape memory effect in antiferroelectric single crystals. The nanoscale structural model and mesoscopic domain evolution are given. The shape memory effect in antiferroelectric single crystals stems from a thermally-induced or electric-field-induced antiferroelectric-ferroelectric phase transformation.

Shape memory effect (SME) was observed not only in special polymers and alloys, but also in polycrystalline ceramics.[6] The SME in alloys results from a thermal- or stress-induced "martensitic" phase transformation. For the AFE materials, once the FE state is induced by applying an electric field, this induced FE phase remains even if the field is removed, corresponding to the "shape memory" phenomenon. Here, the mechanism for the SME in the PLZST AFE single crystals is schematically shown in Fig. S11. Clearly, the SME in PLZST AFE single crystals originates from the thermal- and electric field-induced phase transformations between AFE and FE states.

7: Explanation of the appearance of first cycle and double *P–E* hysteresis loops using the two-instability model

In the main text, the irreversible and reversible antiferroelectric-ferroelectric phase transitions have been explained using the two-instability model for antiferroelectricity. Another features of such phase transitions are the observed first cycle and double *P–E* hysteresis loops. To capture the main features of the observed *P–E* hysteresis loops, we demonstrate how the *P–E* loops can be explained by using the same model. Here, in order to describe the AFE state and electric field-induced FE state, the PLZST crystal is divided into two sublattices (labeled by *a* and *b* with neighboring spontaneous polarizations P_a and P_b, respectively). If P_a and P_b are parallel to each other, revealing the low-temperature FE state. On the other hand, if P_a and P_b are antiparallel and the crystal will exhibit an AFE state. Thus, the FE polarization order parameter P and AFE structural order parameter q can be defined as:[7]

$$P = (P_a + P_b),\ q = (P_a - P_b) \tag{S1}$$

Then, the three-dimensional (3D) Landau free energy of the system contains up to sixth-order AFE and FE polarization parameters and the cross term due to the coupling between AFE and FE can be written as:[8]

$$\begin{aligned}\Delta F = {} & \{\alpha_1(P_1^2+P_2^2+P_3^2)+\alpha_{11}(P_1^4+P_2^4+P_3^4)+\alpha_{111}(P_1^6+P_2^6+P_3^6)+\alpha_{12}(P_1^2P_2^2+P_2^2P_3^2+P_3^2P_1^2)\\ & +\alpha_{112}[P_1^4(P_2^2+P_3^2)+P_2^4(P_1^2+P_3^2)+P_3^4(P_1^2+P_2^2)]+\alpha_{123}P_1^2P_2^2P_3^2\}+\{\beta_1(q_1^2+q_2^2+q_3^2)\\ & +\beta_{11}(q_1^4+q_2^4+q_3^4)+\beta_{111}(q_1^6+q_2^6+q_3^6)+\beta_{12}(q_1^2q_2^2+q_2^2q_3^2+q_3^2q_1^2)\\ & +\beta_{112}[q_1^4(q_2^2+q_3^2)+q_2^4(q_1^2+q_3^2)+q_3^4(q_1^2+q_2^2)]+\beta_{123}q_1^2q_2^2q_3^2\}+\mu_{11}(P_1^2q_1^2+P_2^2q_2^2+P_3^2q_3^2)\\ & +\mu_{12}[P_1^2(q_2^2+q_3^2)+P_2^2(q_1^2+q_3^2)+P_3^2(q_1^2+q_2^2)]+\mu_{44}(P_1P_2q_1q_2+P_2P_3q_2q_3+P_1P_3q_1q_3)\end{aligned} \tag{S2}$$

where α_1, α_{11}, α_{12}, α_{112}, and α_{123} are the FE Landau coefficients, β_1, β_{11}, β_{12}, β_{112}, and β_{123} correspond to the AFE Landau coefficients, μ_{11}, μ_{12}, and μ_{44} mean the couplings between AFE and FE polarizations. In the FE rhombohedral phase, the solutions of interest to Eq. (S2) are $P_1^2 = P_2^2 = P_3^2 = \frac{1}{3}P^2 \neq 0$, and $q_1^2 = q_2^2 = q_3^2 = 0$. In the AFE tetragonal phase, the solutions of interest to Eq. (S2) are $P_1^2 = P_2^2 = P_3^2 = 0$, and $q_1^2 = q_2^2 = q^2 \neq 0$, $q_3^2 = 0$. Thus, the free energy of the system can be expressed as a Landau expansion and rewritten as:

$$\Delta F(T,\ P,\ q, E) = A(T - T_d)P^2 + BP^4 + CP^6 + \gamma(T - T_0)q^2 + \xi q^4 + \zeta q^6 + \delta(T)P^2q^2 - EP \tag{S3}$$

where T_d and T_0 are the depolarization temperature and extrapolated instability temperature for the antiferroelectric-paraelectric phase transition, respectively. $A = \frac{\alpha_1}{(T - T_d)}$, $B = \frac{\alpha_{11} + \alpha_{12}}{3}$, $C = \frac{3\alpha_{111} + 6\alpha_{112} + \alpha_{123}}{27}$, $\gamma = \frac{2\beta_1}{(T - T_0)}$, $\xi = 2\beta_{11} + \beta_{12}$, $\zeta = 2\beta_{111} + 2\beta_{112}$, and $\delta(T) = \frac{2}{3}\mu_{11} + \frac{2}{3}\mu_{12} + \frac{1}{3}\mu_{44}$. According to the the first order phase transition theory,[9] we then derive the equation of state for q

$$\gamma(T - T_0) + 2\xi q^2 + 3\zeta q^4 = 0 \tag{S4}$$

and

$$q_0 = -\frac{\xi}{2\zeta} \tag{S5}$$

$$\gamma(T_A - T_0) = \frac{\xi^2}{4\zeta} \tag{S6}$$

where q_0 means the the spontaneous value of the structural order parameter q at the transition temperature (T_A). A polarization can be induced by the application of electric field E, and then changing the Eq.(S3) to the following:

$$\gamma(T - T_0) + 2\xi q^2 + 3\zeta q^4 + \delta(T)P^2 = 0 \tag{S7}$$

The equilibrium value of P can be obtained by solving the thermodynamic stability conditions $\frac{\partial F}{\partial P} = 0$, which satisfies the equation of state:

$$[A(T - T_d) + 2BP^2 + 3CP^6 + \delta(T)q^2]P = E \tag{S8}$$

When the field-induced transition temperature cools from T_A down to temperature T, the field-induced polarization (P_C) can be obtained by combining equations (S6) and (S7)

$$P_C = \sqrt{\frac{\gamma(T_A - T)}{\delta(T)}} \tag{S9}$$

The field-induced critical phase transition electric field, E_C, following from equations (S4), (S7), and (S8), is given by

$$E_C = \sqrt{\frac{\gamma(T_A - T)}{\delta(T)}}A(T - T_d) + \frac{2\gamma B(T_A - T)}{\delta(T)} + \frac{3\gamma^2 C(T_A - T)}{\delta(T)^2} - \frac{\delta(T)\xi}{2\zeta} \tag{S10}$$

For the antiferroeelctric phase at $T < T_A$, the state with $q = 0$ is energetically favorable for $E > E_C$, while the state with $q \neq 0$ is favorable for $E < E_C$. Thus, for $E < E_C$ the induced

polarization P is very small, the dielectric response of the antiferroeletgric system is given by the relationship below:

$$A(T - T_d)\frac{\delta(T)\xi}{2\zeta}P = E \tag{S11}$$

while for $E > E_C$, dielectric response of the system is controlled by the set of equations (S6) and (S7). This situation may be different. If $T < T_d$, the metastable field induced FE phase can not recover back to AFE phase. Therefore, a first cycle like *P–E* hysteresis loop is apparent. If $T_d < T < T_A$, the field induced FE phase can transform back to AFE phase. One finds that an "antiferroelectric" like *P–E* hysteresis loop is obtained by taking into account the coexistence of AFE and FE phases around E_C.

8: Mechanism of antiferroelectric domain formation

In principle, the domain formation is correlated with the total free energy (F_{Tot}) minimization in the crystal.[10] The total energy may be represented as:

$$F_{Tot} = \Delta F + F_V + F_W \quad \text{(S12)}$$

where ΔF is the Landau free energy given by equation (S2), F_V mainly denotes the elastic energy, and F_W represents the domain wall energy in the antiferroelectric crystal. The elastic energy is:

$$F_V = \frac{1}{2} c_{ijkl}(\varepsilon_{ij} - \varepsilon_{ij}^0)(\varepsilon_{kl} - \varepsilon_{kl}^0) \quad \text{(S13)}$$

where c_{ijkl} is the elastic stiffness. The spontaneous strain is caused by polarization $\varepsilon_{ij}^0 = Q_{ijkl} P_k P_l + \lambda_{ijkl}(q_k q_l - q_k^0 q_l^0)$, where q^0 is the initial antiferro-polarization of reference state, Q_{ijkl} and λ_{ijkl} are the electrostrictive coefficients. The domain wall energy is proportional to the number (n) of domain walls:[11]

$$F_W = n A_W \chi \quad \text{(S14)}$$

where A_W is the area of the walls and χ is the wall energy density. In order to understand the mechanism of antiferroelectric domain formation, the normal tetragonal ferroelectric case is taken into consideration. In terms of normal tetragonal ferroelectrics, the total free energy profile is double well (Fig. S12). Here, the tetragonal domains at "–*P*" (left) and "+*P*" (right) polarization states are schematically shown in the inset of Fig. S12a. Note that only one (left or right) of tetragonal domains is always observed experimentally at a certain polarization state in the tetragonal ferroelectric single crystals. For the tetragonal antiferroelectric single crystal, the predicted total free energy profile is single well (Fig. S12b). The net polarization of an antiferroeletric crystal is equal to zero, as such, antiferroelectric domains tend to form a mixed domain state (± *P*) intertwined with each other (see the left inset of Fig. S12b). Actually, there may be coarse domains in the crystal to minimize the elastic energy. This mixed domain pattern has the possibility to form a square-net domain configuration (see the right inset of Fig. S12b) with the consideration of total free energy minimization. The square-net domain pattern is energetically stable, which can be newly reconstructed during the electric field-induced antiferroelectric to ferroelectric and temperature forced antiferroelectric to paraelectric phase transitions. Similar square-net domain pattern intertwined with each other has been found in orthorhombic antiferroelectric single crystals[11] and also observed in $BaTiO_3$ single crystals at temperature slightly below the Curie temperature.[12]

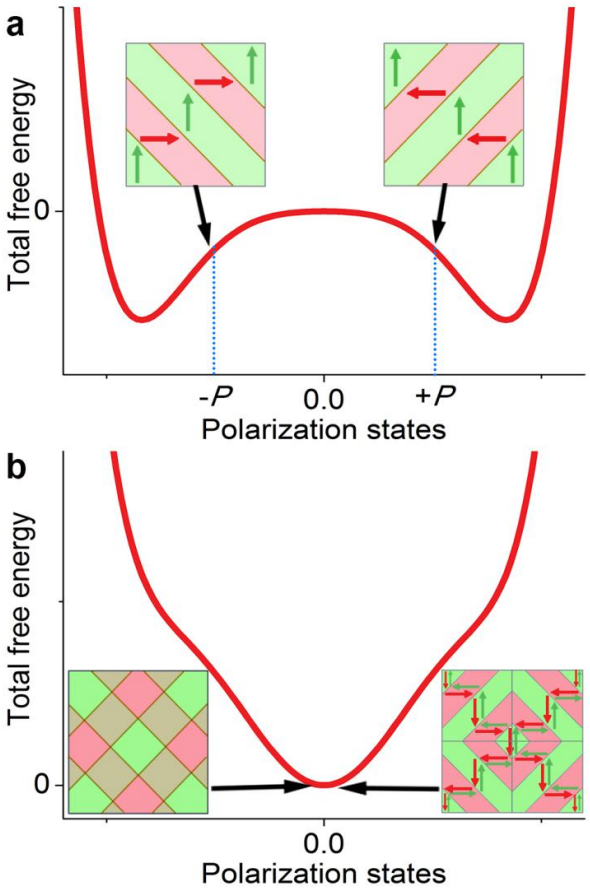

Fig. S12. (a) Schematic representation to explain the tetragonal domains in normal ferroelectric single crystal. The insets show permissible domain states at "–*P*" (left) and "+*P*" (right) polarization states. (b) Predicted total free energy potential of an antiferroelectric single crystal as a function of polarization states. The mixed domain state (left) at zero polarization state, which tends to form a square-net like domain pattern (right).

9: Supplementary Movies

Movie S1: *In situ* domain structure evolution of the PLZST single crystal during the electric field cycling (0–5–0 kV mm^{-1}) at P/A: 0° and P/A: 45° at temperature of 30 °C.

Movie S2: *In situ* domain structure evolution of the PLZST single crystal during the electric field cycling (0–5–0 kV mm^{-1}) at P/A: 0° and P/A: 45° at temperature of 130 °C.

References

1 C. T. Blue, J. C. Hicks, S. E. Park, S. Yoshikawa, L. E. Cross, *Appl. Phys. Lett.* 1996, **68**, 2942–2944.

2 X. H. Hao, J. W. Zhai, L. B. Kong, Z. K. Xu, *Prog. Mater. Sci.* 2014, **63**, 1–57.

3 I. Jankowska-Sumara, M. Podgórna, A. Majchrowski, J. Żukrowski, *J. Therm. Anal. Calorim.* 2017, **128**, 713–719.

4 S. Hong, Handbook of X-ray photoelectron spectroscopy (Perkin-Elmer Corporation, Berlin, 1992).

5 I. Jankowska-Sumara, *Phase Trans.* 2014, **87**, 685–728.

6 K. Uchino, *Actuators* 2016, **5**, 1–23.

7 L. E. Cross, *Philos. Mag.* 1956, **1**, 76–92.

8 B. P. Pokharel, D. Pandey, *Phys. Rev. B* 2002, **65**, 214108.

9 X.-K. Wei, A. K. Tagantsev, A. Kvasov, K. Roleder, C.-L. Jia, N. Setter. *Nat. Commun.* 2014, **5**, 3031.

10 W. W. Cao, G. R. Barsch, *Phys. Rev. B* 1990, **41**, 4334–4348.

11 Y. Li, Q. Li, Q. Yan, Y. Zhang, X. Xi, X. Chu, W. Cao, *Appl. Phys. Lett.* 2012, **101**, 132904.

12 Jr., P. W. Forsbergh, *Phys. Rev.* 1949, **76**, 1187–1201.